ACS OMEGA

http://pubs.acs.org/journal/acsodf

Article

Compensation Effect Exhibited by Gold Bimetallic Nanoparticles during CO Oxidation

Joe Brindle and Michael M. Nigra*

Cite This: *ACS Omega* 2021, 6, 24269−24279

Read Online

ACCESS | Metrics & More | Article Recommendations | Supporting Information

ABSTRACT: While CO oxidation catalyzed by gold nanoparticles has been practiced academically for several decades, there are still important discoveries to be made. One area of current interest is to pair Au with another alloying metal and observe the catalytic consequences of the presence of the other metal. In this work, TiO_2-supported bimetallic Au nanoparticles are alloyed with Cu, Co, Ni, Pd, and Ru and used as catalysts for CO oxidation. Two synthetic methods for the alloys are presented: a strong electrostatic adsorption (SEA) method and a sterically demanding ligand synthesis (SDLS) method which uses triphenylphosphine (TPP) as the ligand. The catalytic performance of the materials synthesized with the SEA and SDLS methods is compared in CO oxidation. The results indicate that the materials tested present an enthalpy−entropy compensation effect. Interestingly, both the enthalpy of activation, $\Delta H^{\ddagger}$, and the entropy of activation, $\Delta S^{\ddagger}$, generally decrease with particle size. AuCo and AuRu materials exhibit a decrease in the overall activity as compared to Au and the other Au alloys when synthesized via SEA. Au face-centered-cubic alloys AuCu, AuNi, and AuPd prepared via SEA show an improvement in activity compared to monometallic Au in our reaction conditions. *In situ* diffuse reflectance infrared Fourier transform spectroscopy presents two distinct regions for Au bimetallics where AuCo and AuRu show peak positions in the region of 2070−2050 cm^{-1}, indicating a weaker interaction for AuCo and AuRu with CO when compared to that of the other alloys. For the SDLS method samples, the hypothesis is that TPP would enhance the CO oxidation rate by enhancing the charge transfer to the metallic surface. The results indicate that SDLS samples have lower CO oxidation rates and if any charge transfer occurs, it is masked by the lateral interactions of the CO π bonds and the phenyl groups of TPP.

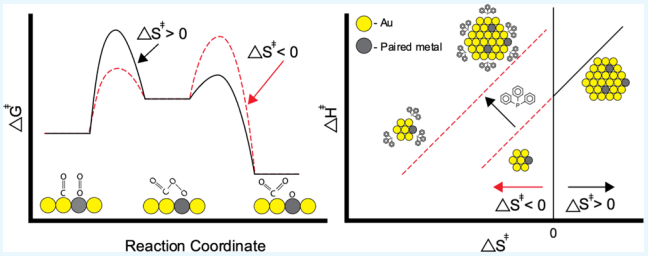

1. INTRODUCTION

Oxidation reactions are some of the most industrially significant reactions, and they present some of the greatest challenges. One of these challenges enables the direct utilization of oxygen from air at ambient temperatures as an oxidant rather than more environmentally hazardous or expensive agents such as peroxides, ozone, and permanganates. Advances in catalytic materials have the potential to facilitate the direct use of air as a benign oxidant in industrial settings. Metallic nanoparticles, particularly gold nanoparticles, have gained considerable attention in catalysis because they exhibit surprising activity and selectivity at low temperatures for oxygen activation.[1−4] One approach to improve the activity of gold nanoparticles is by synthesizing smaller particles. Small particles have the advantage of a higher fraction of surface atoms per mass of metal content, and within this population of surface atoms, undercoordinated sites are often responsible for most of the observed catalytic activity.[1,5−7]

Additionally, the metallic composition affects the catalytic activity of multimetallic nanoparticles. For example, AuPd nanoparticles are active for selective oxidation of methane to produce methanol or syngas, while the monometallic counterparts are inactive.[8] The coupling of metals in a bimetallic nanoparticle may also introduce strain and result in strained active sites. Strained, undercoordinated sites have been suggested as a potential strategy to break kinetic scaling relationships in transition metal nanoparticles.[9−12] Scaling phenomena are the relationships between two energy differences. The first is the difference of energies between the products and reactants of a single reaction mechanism step. The second is the difference between the energy of the transition state and the reactants' energy for that same step. The relationship is generally linear for equivalent reactants and products but depends on the metals selected.[13] Deviations from these scaling relationships may allow for new opportunities in catalysis. Necessarily, there are enthalpic ($\Delta H^{\ddagger}$) and entropic ($\Delta S^{\ddagger}$) contributions to the energy of each transition state. The catalytic material selection changes the

Received: August 7, 2021
Published: September 9, 2021

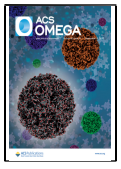

https://doi.org/10.1021/acsomega.1c04236
ACS Omega 2021, 6, 24269−24279

transition state energies; therefore, bimetallic nanoparticles can alter the kinetics by altering the transition state energies, and we can directly compare multiple catalytic materials by comparing the transition state energies.

Comparing multiple catalytic materials for similar reactions can give rise to a unique phenomenon. The phenomenon is a linear relationship between the $\Delta H^{\ddagger}$ and the $\Delta S^{\ddagger}$ of the transition state, known as the enthalpy−entropy compensation effect (EECE). There is a debate as to the physical meaning of this as some dismiss the phenomenon as serendipity due to statistical errors.[14−17] Others suggest that the relative change in the energies of the reaction intermediates or Hinshelwood-like models that adjust for vibrational modes of the activated complex accounts for the observed linearity.[14] In either case, there is a necessity for careful examination of what the enthalpy and entropy compensation among similar materials implies. However, if a single material deviates from this relationship for a similar reaction, there is a unique attribute to consider.[15,18] Even if the enthalpy−entropy compensation displays linearity, all materials in that compensation relationship cannot be assumed to be chemically similar. Therefore, further characterization is pragmatic and necessary for future catalyst design.

Alloying is not the only proposed method to improve catalytic performance. Other modifiers such as organic ligands or other metallic cations may promote the reaction through charge transfer or intermediate stabilization. Organic ligands are often used in the synthesis of metallic nanoparticles in solution to stabilize the nanoparticles against aggregation.[19] When metallic nanoparticles synthesized in solution are immobilized onto support materials, the ligands are generally removed through thermal or chemical processes. For the ligands that still remain on the surface of the nanoparticle, they can have an effect on the catalyst's performance. The ligand's presence can provide a subtle, yet significant, contribution to the activity as a Lewis acid or a Lewis base. Some have suggested that electron donation or electron withdrawal via the ligand may change the activation energy barrier for reactions.[20−25] In this work, we offer two synthetic procedures to prepare TiO_2-supported gold bimetallic nanoparticles; strong electrostatic adsorption (SEA) and sterically demanding ligand synthesis (SDLS). In SEA, aqueous metal cations are electrostatically attracted to a negatively charged support material under specific pH conditions. Metallic nanoparticles are formed from the reduction of the dispersed metal cations. This procedure does not utilize stabilizing ligands, which results in ligand-free nanoparticles immobilized directly onto the support material.[19,26−29] SDLS nanoparticles are prepared first in solution with bound triphenylphosphine (TPP) and retain TPP on the nanoparticle surface when immobilized onto the support.[30,31] We hypothesize that TPP will act as an electron donor to the nanoparticles.[32] It has been proposed that negatively charged Au atoms can act as O_2 activation sites.[33,34] It is of particular interest in this work to determine if the ligand acts as a promoter, a poison, or a benign observer.

CO oxidation is a baseline reaction for measuring the catalytic activity of gold nanoparticles. In addition, CO oxidation activity has broader applications to the activation of oxygen in aerobic conditions. The goals of this study are to (1) synthesize small bimetallic gold nanoparticles using SEA and SDLS preparation methods, (2) determine the dependence of the transition state energy on the particle size, (3) decipher the role of the paired metal in the transition state energies for CO oxidation, (4) elucidate the catalytic role of a Lewis base, the sterically demanding ligand TPP, and (5) determine the stability of each prepared material. This study provides a comparison of SEA and SLDS procedures in terms of the structure and function of supported bimetallic catalysts in CO oxidation.

2. RESULTS AND DISCUSSION

2.1. Materials Characterization with UV−Vis Spectroscopy and Transmission Electron Microscopy. A useful technique to probe the electronic nature of the synthesized nanoparticles is by observing the surface plasmon resonance (SPR) using UV−visible spectroscopy.[35−37] The spectral absorption of visible light is due to the electronic transition from the d to sp valence bands of nanoparticles, which correlate to the nanoparticle size, shape, and composition. In these materials, the SPR band is present at 500−550 nm in both the SDLS-synthesized materials and the SEA-synthesized materials, as shown in Figure 2. The SEA

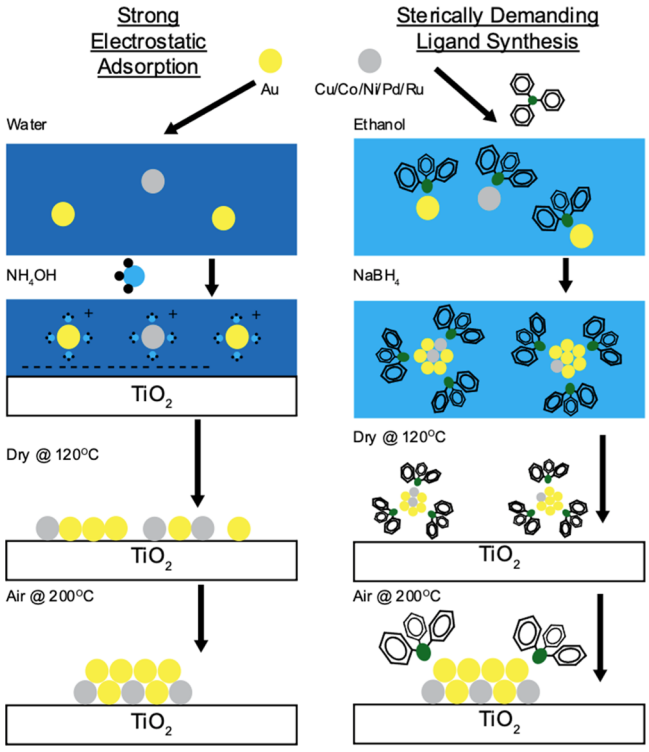

Figure 1. Conceptual diagram of the two synthesis procedures for metallic nanoparticles supported on TiO_2, SEA (left) and SDLS with TPP (right). SEA nanoparticles are prepared by reacting a metallic salt with ammonia, which are then electrostatically attracted to the support surface. The metallic species are then reduced on the support. The SDLS-synthesized nanoparticles are prepared with the TPP ligand before deposition onto the support material.

materials present SPR peaks shown in Figure 2A at values of 526 nm for Au, 537 nm for AuCo, 518 nm for AuCu, 533 nm for AuNi, and 546 nm for AuRu. However, there is no defined peak present for AuPd, but a shoulder is present at approximately 520 nm. The SDLS-synthesized particles have a steeper rise in the region of ∼480 nm, as shown in Figure 2B. An exception is AuCo, which has an SPR band at approximately 545 nm. This steeper rise is due to the presence of the TPP ligand. There are two possible explanations for the steep increase associated with the SDLS. First, the spectra are

https://doi.org/10.1021/acsomega.1c04236
ACS Omega 2021, 6, 24269−24279

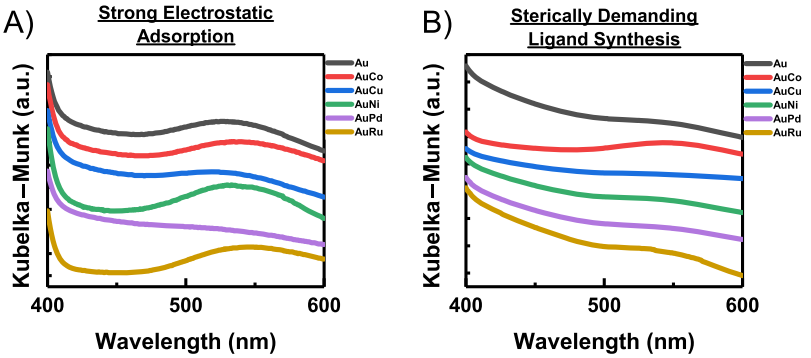

Figure 2. TiO_2-supported Au (black), AuCo (red), AuCu (blue), AuNi(green), AuPd (purple), and AuRu (gold) SPR bands presented for (A) SEA and (B) SDLS. SEA presents clear SPR bands, while SDLS presents shoulders in the range of SPR bands. DR–UV–vis samples are taken following heat treatment in air at 200 °C. Spectra are offset vertically for clarity.

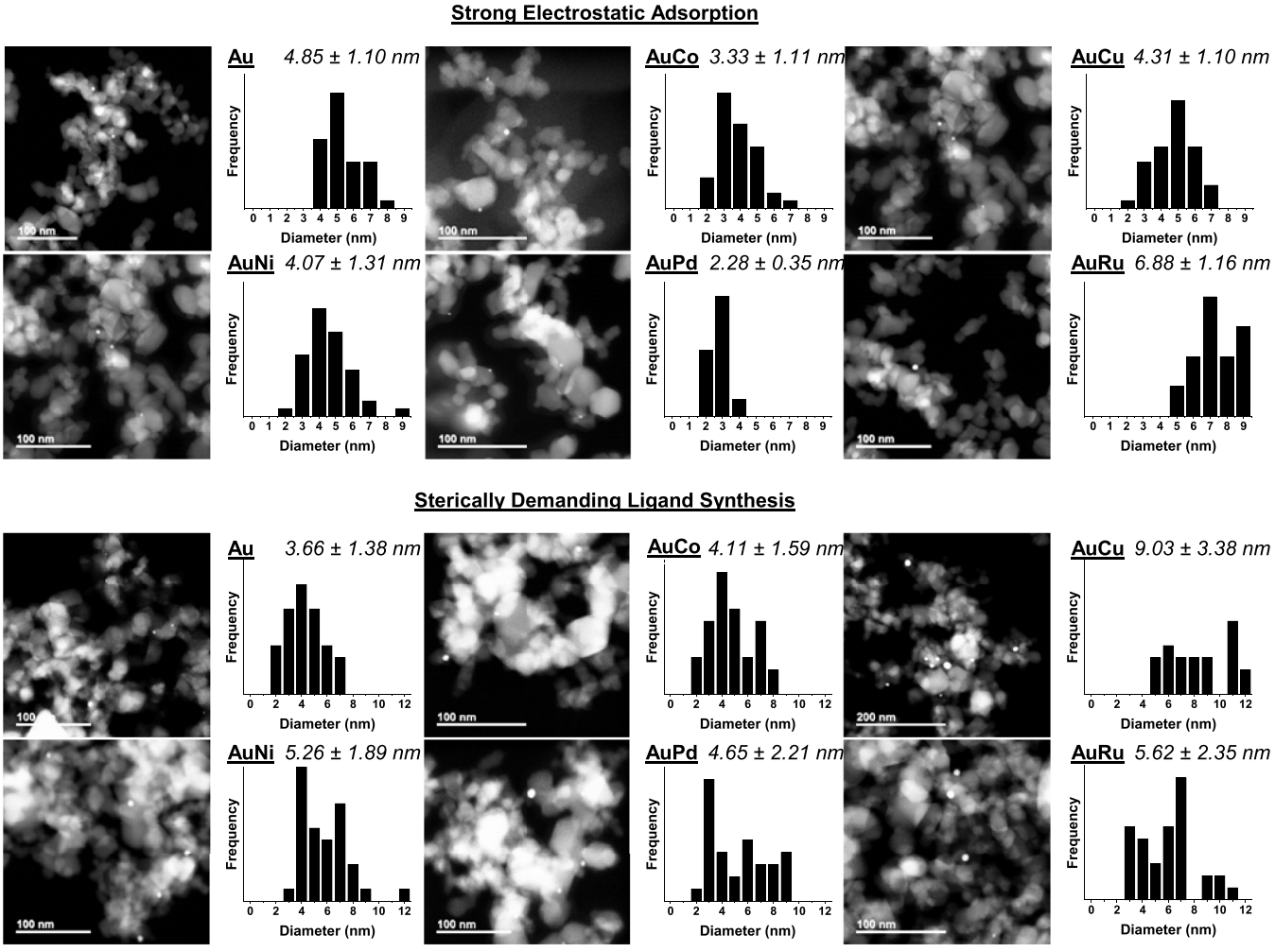

Figure 3. HAADF-STEM images for each bimetallic alloy presented with their respective particle size distributions and average particle sizes after deposition on TiO_2 and heat treatment at 200 °C.

linear combinations of the optical absorption of TPP and the nanoparticles. There are particle sizes of less than 2 nm present in the samples, which do not give a well-defined SPR band and are absorbed at lower wavelengths as they are similar to molecular absorptions.[32] Evidence for these small particles is found in the UV–vis spectra of the metallic nanoparticles after synthesis shown in Figure 2B, where there is an absence of the SPR band and absorption at wavelengths less than 450 nm, which are typical of small particles <2 nm in size.[38,39] The ambiguity of the analysis of the UV–vis spectra remains; therefore, transmission electron microscopy (TEM) is the more accurate method to determine the particle sizes.

High-angle annular dark-field scanning transmission electron microscopy (HAADF-STEM) confirms average particle sizes of greater than 2 nm for all particles made via SDLS following dispersion on TiO_2 and heat-treated under air for 2 h at 200 °C, as shown in Figure 3. This indicates that heat treatment leads to particle aggregation in the SDLS samples. SEA

https://doi.org/10.1021/acsomega.1c04236
ACS Omega 2021, 6, 24269–24279

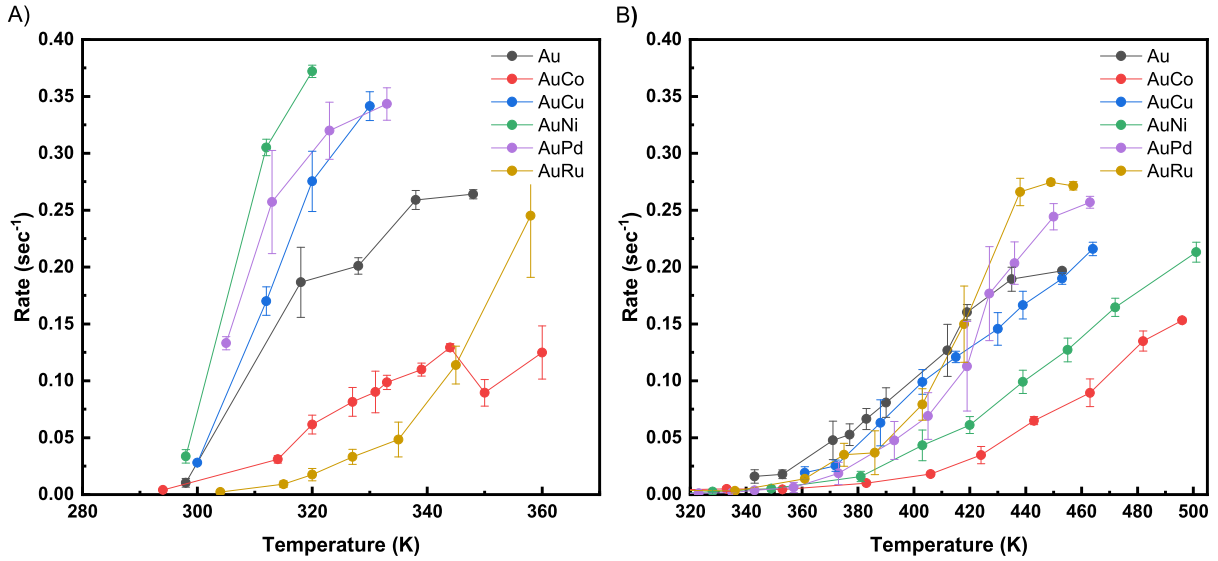

Figure 4. Light-off curves for CO oxidation with Au (black), AuCo (red), AuCu (blue), AuNi (green), AuPd (purple), and AuRu (yellow) for (A) SEA-synthesized and (B) SDLS-synthesized metallic nanoparticles. Rates are expressed as sec^{-1} to simplify mmol CO/mmol (Au + paired metal)/sec. The total gas flow rate is 25 mL/min, the standard volumetric flow rate with 2% CO, 20% O_2, and the balance He at 1 atm. The gas hourly space velocity for this system is 25,380 h^{-1}.

synthesis presents particle sizes with narrower distributions and overall lower sizes after heat treatment. Gold anneals to TiO_2 with little aggregation, suggesting a strong surface interaction of Au and TiO_2.[40] This evidence indicates that the ligand-coated nanoparticle is favored to be mobile on the TiO_2 surface and to aggregate rather than anneal to TiO_2. The propensity to diffuse and aggregate is likely due to the nonpolar phenyl groups that are not likely to interact strongly with the metal oxide's locally charged surface. Particle sizes for SDLS are larger than that of SEA materials after deposition and heat treatment except for monometallic Au nanoparticles and AuRu nanoparticles.

2.2. CO Oxidation Activity Measurements. SEA-prepared catalysts show activity at near room temperature (Figure 4A) for CO oxidation. In contrast, SDLS-prepared catalysts (Figure 4B) do not show significant activity until ~360 K (87 °C). This is likely due to TPP that is still bound to the metal nanoparticle surface. 360 K is approximately the same as the melting temperature for the capping ligand [T_m(TPP) = 353 K], suggesting that below 360 K, a solid phase of ligands forms a barrier to the active sites on the nanoparticles. Above TPP's melting point, TPP is more mobile and allows for mass transfer of the reaction gases to the metallic nanoparticle surface. At high temperatures, rates flatten as conversion approaches 1 (Figure 4 and Figures S1 and S2 in the Supporting Information). Thermogravimetric analysis (TGA) is used to determine that TPP does not volatilize until 523 K (Figure S6).

The metallic composition of the catalysts affects their CO oxidation activities. SEA-prepared Au, AuCu, AuNi, and AuPd catalysts show activity at ~300 K, while AuCo and AuRu demonstrate activity at ~320 K. Generally, phase diagrams for bulk AuCo and AuRu indicate that the metals are immiscible at the temperatures observed. Au has a face-centered-cubic (fcc) structure at these temperatures, while Ru and Co have hexagonal close-packed (hcp) structures. However, metals can become miscible in nanoparticles due to the relative surface energy differences in the metals.[41] From inductively coupled plasma mass spectrometry (ICP−MS) elemental analysis, Au contents are measured to be 80.0% and 95.5% for AuCo and AuRu, respectively, suggesting that the likely bimetallic structure is fcc with Ru-substitution within the Bravais lattice.[42] The results show that for all tested fcc metals alloyed with Au, the activity is better than that of monometallic Au nanoparticles when using the SEA synthesis method. It is observed that for the fcc metals alloyed with gold, the activity increases as the particle size decreases, with the exception of the AuPd nanoparticles. One may predict that the smaller particle size of AuPd would lead to the best activity. However, AuPd shows a slightly lower rate of 0.257 ± 0.045 s^{-1} than the highest rate of AuNi at 0.305 ± 0.007 s^{-1} at about 310 K. This indicates that particle size is not solely responsible for the differences in CO oxidation activity. The SDLS method shows that AuCo and AuNi exhibit the lowest activity, while the activities of Au, AuCu, AuRu, and AuPd are not significantly different. Overall, the CO oxidation activity for the SDLS catalysts is less than that of the SEA catalysts. There does not appear to be a clear relationship between the particle size and CO oxidation activity for the SDLS-synthesized materials. As an example, AuNi and AuRu have similar particle sizes when synthesized via SDLS but lie on the opposite ends of the activity spectrum. For SEA-synthesized AuNi and AuRu, AuNi is among the most active materials, but for SDLS-synthesized AuNi and AuRu, AuRu is one of the most active catalysts. It appears from this data that the presence or absence of TPP has an effect on the CO oxidation performance of the AuNi and AuRu catalysts. In terms of the catalytic performance of these materials, it is useful to think of them in three categories: SDLS Au alloys, SEA-prepared Au-fcc alloys, and SEA-prepared Au-hcp alloys.

2.3. Compensation Effect in Bimetallic Nanoparticles. CO oxidation is used as a probe reaction to compare the thermodynamics of the transition state for each catalyst material through the Arrhenius Equation (eq 1) and bimolecular Eyring equation (eq 2).

https://doi.org/10.1021/acsomega.1c04236
ACS Omega 2021, 6, 24269−24279

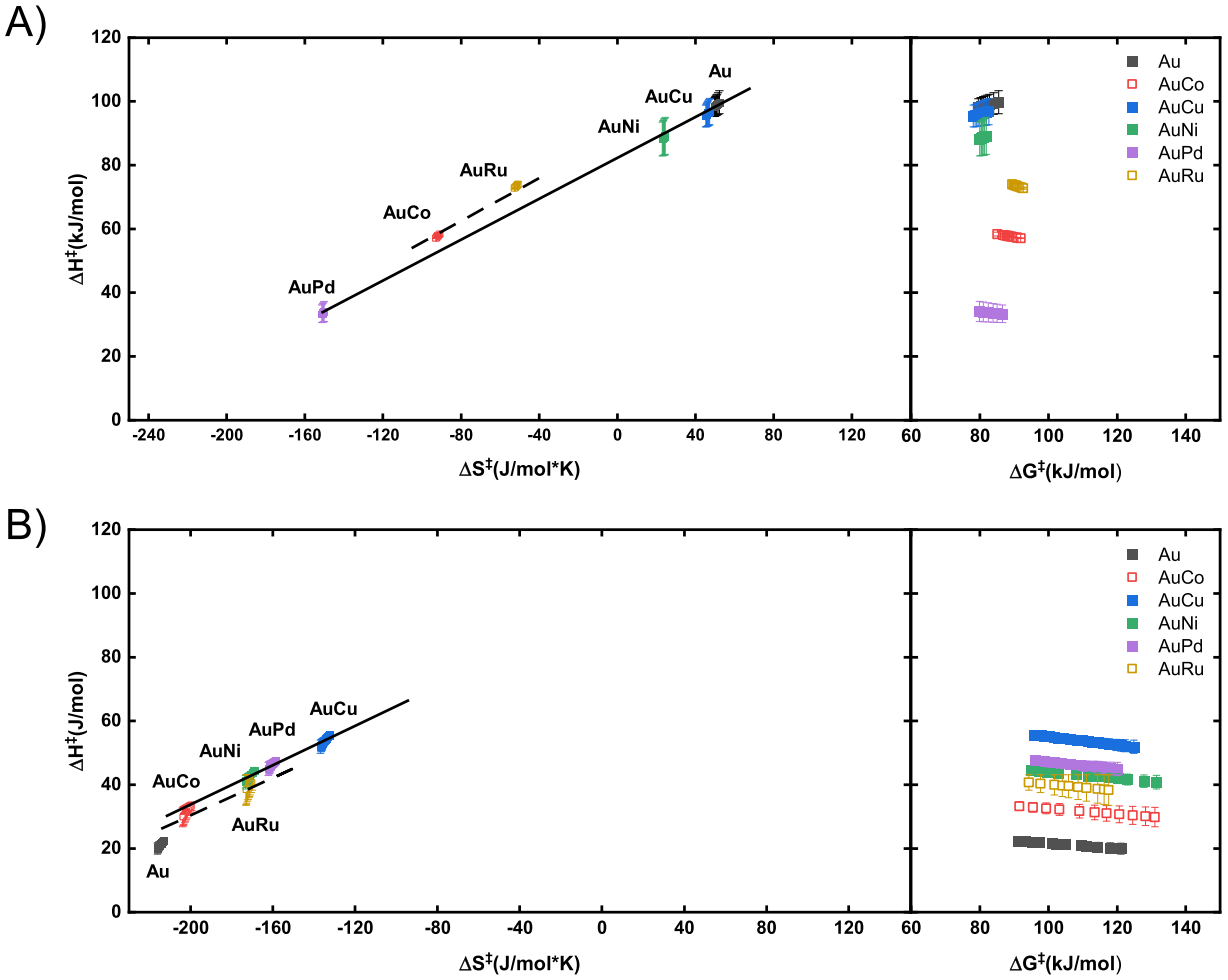

Figure 5. $\Delta H^{\ddagger}$ and $\Delta S^{\ddagger}$ for SEA (A) and SDLS (B) procedures for Au (gray), AuCo (red), AuCu (blue), AuNi (green), AuPd (purple), and AuRu (gold). Trend lines are shown for Au-fcc metals (solid) and Au-hcp (dashed) SEA-prepared metals and SDLS metals. Au-fcc bimetallics are denoted as solid shapes, and Au-hcp bimetallics are denoted as hollow shapes. $\Delta G^{\ddagger}$ is determined by eq 3 for all reaction temperatures.

$$k = A \exp\left(-\frac{E_a}{RT}\right) \tag{1}$$

$$k = \left(\frac{k_b T}{h}\right)(RT)\exp\left(-\frac{\Delta G^{\ddagger}}{RT}\right) \tag{2}$$

$$\Delta G^{\ddagger} = \Delta H^{\ddagger} - T\Delta S^{\ddagger} \tag{3}$$

Equations 1 and 2 are comparable as they are of similar forms. Transition state Gibbs free energy is a combination of the enthalpy and entropy of transition, as determined by eq 3.

Figure 5 presents the calculated enthalpy ($\Delta H^{\ddagger}$), entropy ($\Delta S^{\ddagger}$), and Gibbs free energy ($\Delta G^{\ddagger}$) of transition of the monometallic Au and Au alloys for CO oxidation. The Supporting Information contains details on the calculations of these thermodynamic values. There is a linear trend between $\Delta H^{\ddagger}$ and $\Delta S^{\ddagger}$ for the catalysts that are tested in this work. This linear trend is indicative of the EECE, which means that a similar chemical process is occurring on these materials. For the SEA-synthesized materials in Figure 5A, Au, AuCu, AuNi, and AuPd all lie along the same line with $\Delta G^{\ddagger}$ values of 80−83 kJ/mol for the temperature range studied in this work. The similar values for $\Delta G^{\ddagger}$ over a range of particle sizes for the SEA-synthesized Au-fcc alloys, as shown in Figure 6, illustrate that the particle size is not always the only determining factor in CO oxidation activity. Metallic composition also plays an important role in addition to the particle size. An analogous observation can be made for the SEA-synthesized Au-hcp alloys. AuCo and AuRu have different particle sizes but have similar $\Delta G^{\ddagger}$ values, which translates into similar CO oxidation activities. The SEA-synthesized Au-hcp alloys exhibit a higher $\Delta G^{\ddagger}$ of 88−90 kJ/mol than the SEA-synthesized Au-fcc alloys for the same temperature range. This higher $\Delta G^{\ddagger}$ is consistent with the lower CO oxidation activity that is observed for the SEA-synthesized AuCo and AuRu materials versus the Au-fcc alloys.

Figure 5B shows the calculated $\Delta H^{\ddagger}$, $\Delta S^{\ddagger}$, and $\Delta G^{\ddagger}$ values of the SDLS-synthesized monometallic Au and Au alloys for CO oxidation. $\Delta G^{\ddagger}$ is calculated over the range of temperatures used for the light-off curves in Figure 4. It is observed that the SDLS-synthesized materials have lower $\Delta H^{\ddagger}$ and $\Delta S^{\ddagger}$ than the SEA-synthesized catalysts. A lower $\Delta H^{\ddagger}$ is favorable, but the more negative $\Delta S^{\ddagger}$ has a greater contribution to the higher $\Delta G^{\ddagger}$ of 90−130 kJ/mol that is observed for the SDLS catalysts. The higher $\Delta G^{\ddagger}$ that is observed for the SDLS materials is consistent with the lower CO oxidation activity for the SDLS materials when compared to that of the SEA materials. The observation lends further support to the idea that TPP may be acting as a poison in the SDLS catalysts.

https://doi.org/10.1021/acsomega.1c04236
ACS Omega 2021, 6, 24269−24279

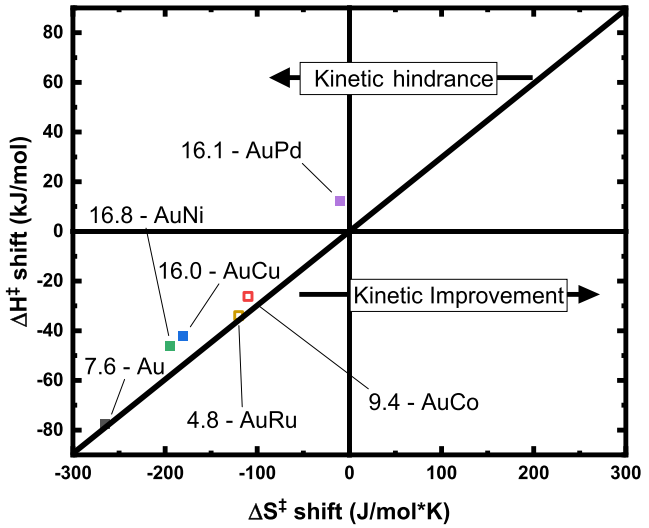

Figure 6. Shifts in $\Delta H^{\ddagger}$ and shifts in $\Delta S^{\ddagger}$ due to the presence of TPP ligands. Values are calculated by $\Delta H^{\ddagger}$ shift = $\Delta H^{\ddagger}_{i,SDLS} - \Delta H^{\ddagger}_{i,SEA}$ and $\Delta S^{\ddagger}$ shift = $\Delta S^{\ddagger}_{i,SDLS} - \Delta S^{\ddagger}_{i,SEA}$. The line denotes no change in $\Delta G^{\ddagger}$ values between the SEA and SDLS methods. The numbers associated with each point are the increase in $\Delta G^{\ddagger}$ between the SDLS-synthesized particles and the SEA-synthesized particles. Colors indicate materials: Au (black), AuCo (red), AuCu (blue), AuNi (green), AuPd (purple), and AuRu (gold).

Figure 6 is a graphical representation of the differences in $\Delta H^{\ddagger}$, $\Delta S^{\ddagger}$, and $\Delta G^{\ddagger}$ values between the SEA and SDLS samples. The abscissa represents the difference in $\Delta S^{\ddagger}$ values between the SEA- and SDLS-prepared samples for each alloy composition. The $\Delta S^{\ddagger}$ shift is defined as $\Delta S_{SDLS}{}^{\ddagger} - \Delta S_{SEA}{}^{\ddagger}$. The ordinate is the $\Delta H^{\ddagger}$ shift, which is equal to $\Delta H_{SDLS}{}^{\ddagger} - \Delta H_{SDLS}{}^{\ddagger}$. The black line indicates no change in $\Delta G^{\ddagger}$ at 350 K. Points which lie above the solid black line will indicate a $\Delta G^{\ddagger}$ which is higher for the SDLS sample than that for the SEA-synthesized material for the same alloy, and points which lie below the line indicate a decrease in $\Delta G^{\ddagger}$, which is favorable for catalysis. All of the SDLS-synthesized points lie above the line, which indicates that there is a larger kinetic barrier for activation when using the SDLS-synthesized catalysts than that with the SEA-synthesized catalysts for CO oxidation. The experimental catalysis data in Figure 4 support this conclusion.

Figure 7 shows the relationship between particle size and thermodynamic parameters, $\Delta H^{\ddagger}$, $\Delta S^{\ddagger}$, and $\Delta G^{\ddagger}$. The relationship between $\Delta G^{\ddagger}$ and CO oxidation activity has been discussed in the previous two paragraphs. It is observed that the $\Delta H^{\ddagger}$ and $\Delta S^{\ddagger}$ generally decrease with smaller particle sizes for both the SEA and SDLS methods. Two notable exceptions are AuRu for both synthesis routes and AuNi for the SDLS method. Regarding $\Delta H^{\ddagger}$, in smaller particles, there is a greater proportion of undercoordinated sites that we hypothesize lower the enthalpic threshold for CO oxidation. These undercoordinated sites will favorably provide electron donation to antibonding orbitals and lower the activation barriers. Decreases in $\Delta S^{\ddagger}$ are explained by the higher activation energy for the formation of OCOO intermediates on smaller particles, as observed by Liu et al.[1] It was also observed by Liu et al. that larger particles have higher activation energies for the dissociation of the OCOO intermediate.[1] Undercoordinated sites shift the rate-determining step from the dissociation of oxygen to the association of O_2 and CO. Our results are consistent with these observations.

By analyzing the SDLS-prepared samples, which have lower $\Delta H^{\ddagger}$ and $\Delta S^{\ddagger}$, it is apparent that TPP is having an effect through charge transfer or electron donation to decrease the $\Delta H^{\ddagger}$ and limits the association of CO and O_2 to decrease the $\Delta S^{\ddagger}$. The only variable to account for the drastic difference in the kinetic parameters is the presence of TPP. TPP is likely blocking sites on the metal surface and limiting the locations where CO and O_2 can bind with a favorable geometry to react.

2.4. Fourier Transform Infrared Spectroscopy of Chemisorbed CO. The observation of chemisorbed CO on these materials provides insights into the nature of the active sites. Figure 8 shows a comparison of the different alloys synthesized by the SEA method on the left and the SDLS method on the right. It is observed that the Au-fcc alloys have CO adsorption signals in the range of 2010−1990 cm^{-1}. CO peaks in this range straddle two regions: single-atom linear (2130−2000 cm^{-1}) and two-atom bridging (2000−1880 cm^{-1}) types.[43−46] It is likely that the majority of chemisorbed CO on Au-fcc alloys is of the two-atom bridging type. The work of Evans et al. observes peaks in this region and suggests assigning the peaks to bridging carbonyls on the facets of (100) and (110) surfaces.[47] For the Au-hcp alloys prepared via SEA, the linear chemisorption of CO on AuCo and AuRu is shown with peaks at 2055.7 and 2064.8 cm^{-1}, respectively. The differences observed in the CO chemisorption via Fourier transform infrared (FTIR) spectroscopy between the SEA-synthesized Au-fcc alloys and the Au-hcp alloys indicate that there are different catalytic sites present. These different sites exhibit significantly different catalytic activities for CO oxidation, as shown in Figure 4A. For SDLS-synthesized Au, AuNi, and AuPd, there is a blue shift in chemisorbed CO when comparing these catalysts to the same alloys synthesized via SEA, while there is nearly a 100 cm^{-1} red shift for the SDLS-synthesized AuCu material versus SEA-synthesized AuCu. This large shift suggests a different site that is available on SDLS-prepared AuCu. Additionally, SEA-prepared AuCu has a CO adsorption peak at a much higher frequency (2109.9 cm^{-1}) than the other Au-fcc alloys at around 2000 cm^{-1}, which is further indicative of unique catalytic sites on AuCu. CO adsorption on SDLS-prepared AuCu is strong due to the fact that the chemisorption IR peaks do not recede for AuCu following CO shutoff. The blue shift from the SEA-prepared materials to the SDLS-prepared materials is not expected as it is hypothesized that TPP would donate electron density to the metal surface. To observe the charge transfer from TPP to the nanoparticle, one would anticipate a red shift in chemisorbed CO. The red shift occurs due to the weakening of the CO bond from π back-bonding. The π back-bonding is a result of the electron donation to the valence of the catalytic material. Any favorable enhancement of CO oxidation catalysis when using SDLS-prepared AuCu due to the TPP charge transfer is likely counteracted by the larger particle size and the physical blocking of AuCu by TPP.

Figure 9 shows the relationship between $\Delta H^{\ddagger}$ and the frequencies of the adsorbed CO peaks. SEA-synthesized Au-hcp alloys have peak positions at higher frequencies and lower $\Delta H^{\ddagger}$ values when compared to SEA-synthesized Au-fcc alloys. This lends further evidence to the hypothesis that the active sites for CO oxidation on Au-fcc alloys are different from that of Au-hcp alloys. Just as there was not a clear trend in determining the CO oxidation activity via particle size or thermodynamic values for the SDLS-synthesized materials,

https://doi.org/10.1021/acsomega.1c04236
ACS Omega 2021, 6, 24269−24279

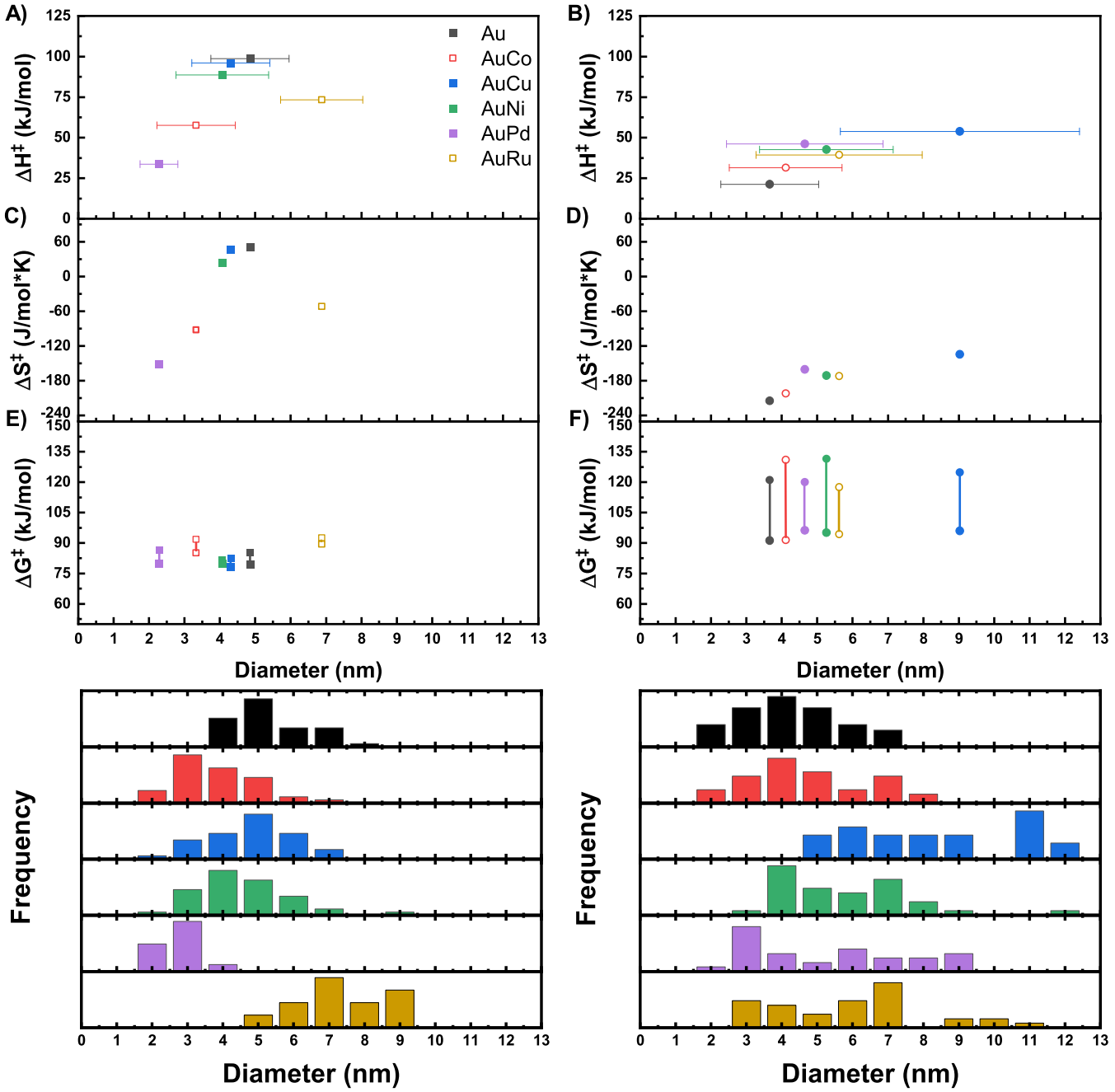

Figure 7. Particle size and $\Delta H^{\ddagger}$ (A,B), $\Delta S^{\ddagger}$ (C,D), and $\Delta G^{\ddagger}$ (E,F) for SEA- (A,C,E) and SDLS-prepared (B,D,F) Au (Black), AuCo (red), AuCu (blue), AuNi (green), AuPd (purple), and AuRu (gold). X-error bars in (A,B) denote the particle size standard deviation, while y-error bars in E and F denote the minimum and maximum of Gibbs free energy of transition for the measured temperature range. Actual particle size distributions are outlined below for simplicity. Au-fcc bimetallics are denoted as solid shapes, and Au-hcp bimetallics are denoted as hollow shapes.

there also does not appear to be a clear trend relating the FTIR CO adsorption peak location and $\Delta H^{\ddagger}$.

2.5. Postcatalytic UV−Vis Characterization. Figure 10 shows the solid-state diffuse reflectance (DR) UV−vis spectra for the samples before catalysis using solid lines and after CO oxidation catalysis using dashed lines. Changes in the shapes of the spectra suggest changes in the energies of the transition from the sp band to the d band for nanoparticles, which may be due to the changes in particle size. For the SEA-synthesized samples, the smallest shifts in the SPR bands are observed in the AuCu, AuNi, and AuPd samples. These samples are some of the most active samples for CO oxidation. When analyzing the SDLS-synthesized samples, there is a decrease in the absorbance in all spectra between 400 and 450 nm, which may be indicative of the loss of TPP or the aggregation of smaller particles during catalysis. AuCo and AuNi samples have the largest shift in the shoulder/peak location of the SDLS-synthesized samples; AuCo and AuNi also have the lowest CO oxidation activities of the SDLS-synthesized samples. We hypothesize based on these UV−vis results that there is nanoparticle aggregation in these samples that contributes to the lower CO oxidation activity when compared to that of the other SDLS-synthesized samples.

https://doi.org/10.1021/acsomega.1c04236
ACS Omega 2021, 6, 24269−24279

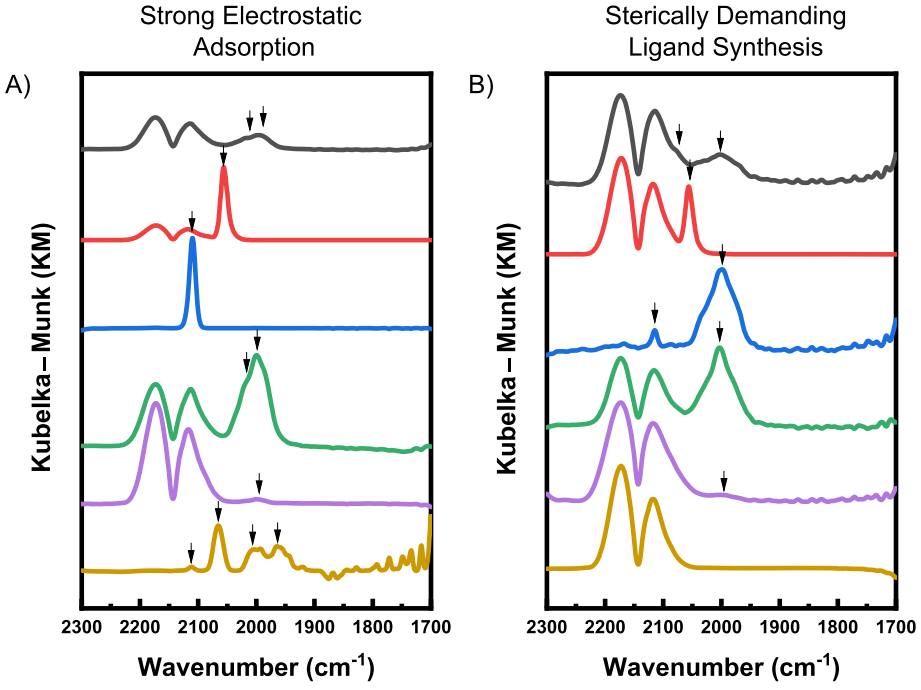

Figure 8. CO adsorption observed by DRIFTS for SEA- (A) and SDLS-prepared (B) Au (black), AuCo (red), AuCu (blue), AuNi (green), AuPd (purple), and AuRu (gold). The system is observed at room temperature with 25 sccm of 5% CO with balance He.

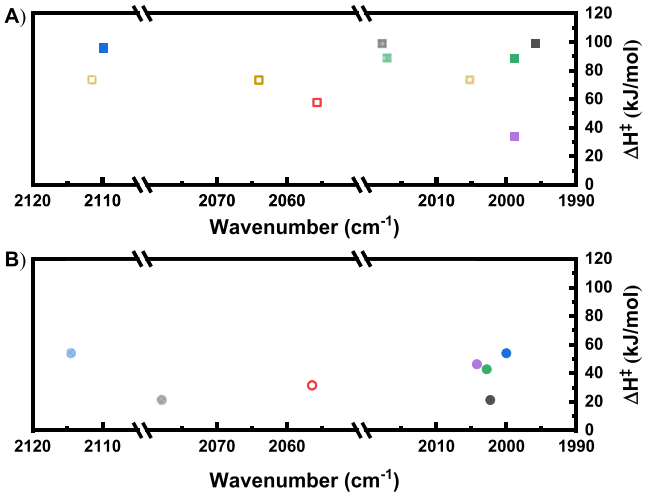

Figure 9. CO chemisorption IR bands relative to $\Delta H^{\ddagger}$ for SEA- (A) and SDLS-prepared (B) Au (black), AuCo (red), AuCu (blue), AuNi (green), AuPd (purple), and AuRu (gold). Au-fcc alloys are solid shapes, and Au-hcp alloys are hollow shapes. Lighter symbols of the same color indicate lower intensity peaks for that material. No peaks were observed for AuRu (SDLS).

3. CONCLUSIONS

This work compares the CO oxidation activity for Au and Au alloy materials which are synthesized via two different methods: SEA and SDLS. The catalytic performance of these materials indicates that they fall into three different categories: SEA-synthesized Au-fcc alloys, SEA-synthesized Au-hcp alloys, and SDLS-synthesized alloys. These materials exhibit the EECE when considering the energetics of their transition states. The lowest $\Delta G^{\ddagger}$ values are observed in SEA-synthesized Au-fcc alloys, followed by SEA-synthesized Au-hcp alloys and, lastly, SDLS-synthesized Au alloys. The CO oxidation rates also follow this same trend with the SEA-synthesized Au-fcc alloys being the most active catalysts and the SDLS-synthesized Au alloys exhibiting the lowest catalytic activity. The smaller particle size generally leads to lower $\Delta H^{\ddagger}$ and $\Delta S^{\ddagger}$ values, which suggests that the associative mechanism is rate-limiting on small particles, while larger particles have higher $\Delta H^{\ddagger}$ and $\Delta S^{\ddagger}$ values that indicate that the dissociative mechanism is rate-limiting on larger particles. DRIFT spectroscopy of chemisorbed CO indicates that there are different sites present on each of the three categories of catalysts based on the location of the CO bands. It was expected that TPP would promote oxidation catalysis through electron donation to the metal surface; instead, the SDLS-synthesized samples exhibited lower CO oxidation rates than their SEA-synthesized counterparts. FTIR spectra indicated no charge transfer between TPP and the metal surface. If charge transfer did occur, then it was masked by the lateral interaction of the CO π bonds and the phenyl groups of TPP. In these materials, it was concluded that TPP acts as a poison by blocking access to the metal surface. Further work is necessary in utilizing organic ligands in heterogeneous catalysis as a means to enhance performance via electron donation/withdrawal from metallic nanoparticle surfaces.

4. METHODS

4.1. Materials. TiO_2 (P25), $HAuCl_4{\cdot}3H_2O$ (99.9%), $Cu(NO_3){\cdot}6H_2O$ (>98%), $PdCl_2$ (99.999%), $Ni(NO_3){\cdot}6H_2O$ (99.999%), TPP (99%), ethanol, and $NaBH_4$ (99.99%) were obtained from Sigma-Aldrich. $RuCl_2{\bullet}H_2O$ (99.99%) was obtained from Alfa Aesar. NH_4OH (20–22% NH_3) was obtained from Fisher Scientific. $Co(NO_3)_2{\cdot}6H_2O$ (99%) was obtained from Acros. Type 1 deionized water is generated with a purity of 18.2 MΩ via a Millipore DirectQ 3 UV water purification unit.

4.2. Sterically Demanding Ligand Synthesis. Au and Au alloy nanoparticles were synthesized using modifications from the methods published by Kapil et al., developed for

https://doi.org/10.1021/acsomega.1c04236
ACS Omega 2021, 6, 24269−24279

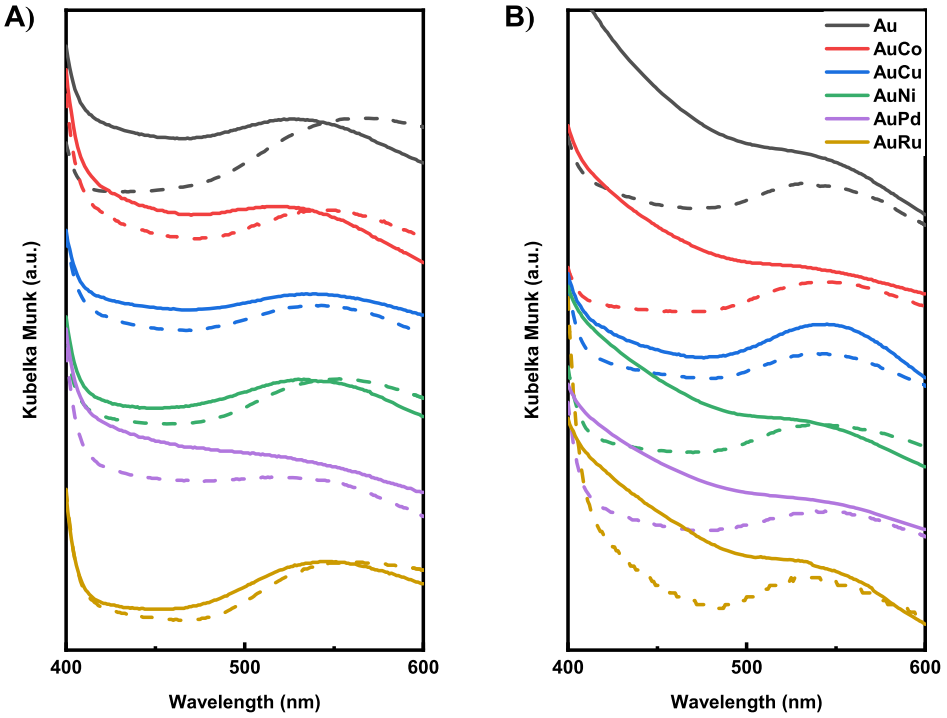

Figure 10. DR UV−vis spectra illustrate aggregation for the (A) SEA- and (B) SDLS-synthesized samples. Solid lines indicate the materials before CO oxidation, and dashed lines indicate materials after CO oxidation. The sample compositions are as follows: Au (black), AuCo (red), AuCu (blue), AuNi (green), AuPd (purple), and AuRu (gold). Note: spectra are scaled and offset to elucidate peak shapes and changes in peak positions.

monometallic Au particle synthesis.[48] A schematic is shown in Figure 1 (right side). 0.015 mmol $HAuCl_4{\cdot}3H_2O$ was dissolved in 30 mL of ethanol in a round-bottom flask. In a separate vessel, 39.3 mg of TPP was dissolved in 15 mL of ethanol. In addition, a third vessel containing 2.3 mg of $NaBH_4$ in 5 mL of ethanol was prepared. After ensuring that all solutions were well-dissolved, the TPP solution was added to the $HAuCl_4{\cdot}3H_2O$ solution. Following 1 min of stirring, the $NaBH_4$ solution was added in its entirety to the TPP−Au solution. The bimetallic SDLS nanoparticles were prepared through the same procedure with a metal solution prepared with a molar ratio of 9:1 (Au/metal) with 0.0135 mmol $HAuCl_4{\cdot}3H_2O$ and 0.0015 mmol of the paired metal. The metal precursors for the paired metal were $Cu(NO_3){\cdot}6H_2O$, $Ni(NO_3){\cdot}6H_2O$, $PdCl_2$, $Co(NO_3)_2{\cdot}6H_2O$, and $RuCl_2{\cdot}H_2O$.

To support these nanoparticles onto TiO_2, 580 mg of TiO_2 was measured and added to the nanoparticle solution and vigorously stirred for 1 h. The expected metal loading was 1 wt %. The solvent was removed via rotary evaporation at 40 °C. The resulting powder was heat-treated to anneal the nanoparticles to TiO_2 in stagnant air overnight at 200 °C. Following the heat treatment process, the powder remained a light orange color.

4.3. Strong Electrostatic Adsorption. SEA synthesis was performed so that the metal loading and the nominal metal composition are similar to those in the SDLS. A schematic is shown in Figure 1 (left side). 23 mL of 18.2 MΩ water was added to a round-bottom flask. 1 mL of 2.93 mM $HAuCl_4{\cdot}3H_2O$ was added to the water, and 1 mL of a 1.79 mM solution of the paired metal was added to the gold solution. Additionally, 5 mL of NH_4OH was added to the metal solution, and the pH was measured and adjusted to 10.3 through the addition of 0.1 M HCl. 1.00 g of TiO_2 was added to the metal solution and was then stirred vigorously for 1 h. The powder was dried for 1 h at 120 °C and then crushed and heat-treated in air overnight at 200 °C.

4.4. UV−Vis Spectroscopy. UV−vis measurements were obtained on a Shimadzu UV-2600 spectrophotometer. All UV−vis characterizations were performed in the spectrum mode scanning from 600 to 200 nm with a step size of 1.0 nm. Liquid UV−vis samples were referenced and baselined with ethanol. DR measurements were obtained with a Harrick Praying Mantis DR chamber with KBr as a baseline and referenced to the intensity of direct transmission.

4.5. Transmission Electron Microscopy. Bimetallic nanoparticles supported on TiO_2 were dispersed in 1.5 mL of ethanol solution and sonicated. A drop of the dispersed solution was drop-cast onto a TEM grid and dried. TEM measurements were obtained in the HAADF-STEM mode with a JEOL JEM 2800 electron microscope with an acceleration voltage of 200 keV. Particle size was determined using ImageJ processing software.

4.6. Thermogravimetric Analysis. TGA was performed by a TA Instruments QT-600 at a temperature ramp of 10 °C/min in nitrogen (300 mL/min) to a final temperature of 400 °C and held for 20 min.

4.7. Diffuse Reflectance Fourier Transform Infrared Spectroscopy. Diffuse reflectance infrared Fourier transform spectroscopy (DRIFTS) was performed with a Thermo Fisher Nicolet IS-50 FTIR instrument equipped with a Harrick Praying Mantis *in situ* characterization chamber and a mercury−cadmium−telluride liquid-nitrogen-cooled detector. Background spectra were taken with 32 scans at 2 cm^{-1} resolution for the catalyst powder using a 20 mL/min He flow. A flow of CO was added at 5 mL/min with the He flow (25 mL/min total) until doublet peaks for gas-phase CO were observed at 2173 and 2116 cm^{-1} and any other peaks in the spectra did not change. The CO flow was then shut off, and

https://doi.org/10.1021/acsomega.1c04236
ACS Omega 2021, 6, 24269−24279

spectra were collected until the gas-phase peaks vanished. Final data were reprocessed to 4 cm^{-1} to smooth the incremental rotational peaks that constitute the two gas-phase peaks at 2173 and 2116 cm^{-1}.

4.8. CO Oxidation. 250.0 ± 0.3 mg of the selected catalyst powder was added to a U-tube quartz reactor with a 1 in. diameter. A 25 mL/min flow consisting of 2% CO, 20% O_2, and the balance He was passed through the catalyst bed at 1 atm absolute. The temperature was brought from room temperature at an increment of about 10 °C. At least three samples were removed by the gas-sampling valve and analyzed via online gas chromatography−MS. The following equation was utilized to determine the rate.

$$\text{Rate} = \dot{V}\frac{y_{co}P}{RT}\left(\frac{1}{m_{cat}L}\right)X \quad (4)$$

$\dot{V}$ is the volumetric flow rate at STP, y_{co} is the feed fraction of CO, P is the pressure, R is the ideal gas constant, T is the temperature in the reactor, m_{cat} is the mass of the catalyst in the reactor, L is the metal loading per mass of the catalyst, and X is the conversion. Equation 4 is applicable to a perfectly mixed reactor; the perfectly mixed reactor assumption is valid under conditions tested due to the wide aspect ratio (diameter/thickness). This results in a residence time that is longer than the axial diffusion time, and the diffusion is fast compared to the residence time.

■ ASSOCIATED CONTENT

Supporting Information

The Supporting Information is available free of charge at https://pubs.acs.org/doi/10.1021/acsomega.1c04236.

Calculation of the energies of transition for all materials, UV−vis spectra, CO oxidation light-off curves, ICP−MS analysis, and TGA of the SDLS-synthesized samples (PDF)

■ AUTHOR INFORMATION

Corresponding Author

Michael M. Nigra − *Department of Chemical Engineering, University of Utah, Salt Lake City, Utah 84112, United States*; orcid.org/0000-0002-0188-0447; Email: michael.nigra@utah.edu

Author

Joe Brindle − *Department of Chemical Engineering, University of Utah, Salt Lake City, Utah 84112, United States*

Complete contact information is available at: https://pubs.acs.org/10.1021/acsomega.1c04236

Notes

The authors declare no competing financial interest.

■ ACKNOWLEDGMENTS

The authors gratefully acknowledge the Department of Chemical Engineering at the University of Utah for their financial support of this work.

■ REFERENCES

(1) Liu, J.-X.; Filot, I. A. W.; Su, Y.; Zijlstra, B.; Hensen, E. J. M. Optimum Particle Size for Gold-Catalyzed CO Oxidation. *J. Phys. Chem. C* **2018**, *122*, 8327−8340.

(2) Min, B. K.; Alemozafar, A. R.; Pinnaduwage, D.; Deng, X.; Friend, C. M. Efficient CO Oxidation at Low Temperature on Au(111). *J. Phys. Chem. B* **2006**, *110*, 19833−19838.

(3) Haruta, M.; Kobayashi, T.; Sano, H.; Yamada, N. Novel Gold Catalysts for the Oxidation of Carbon Monoxide at a Temperature far Below 0 °C. *Chem. Lett.* **1987**, *16*, 405−408.

(4) Pischel, J.; Pucci, A. Low-Temperature Adsorption of Carbon Monoxide on Gold Surfaces: IR Spectroscopy Uncovers Different Adsorption States on Pristine and Rough Au(111). *J. Phys. Chem. C* **2015**, *119*, 18340−18351.

(5) Stratakis, M.; Garcia, H. Catalysis by Supported Gold Nanoparticles: Beyond Aerobic Oxidative Processes. *Chem. Rev.* **2012**, *112*, 4469−4506.

(6) Yudanov, I. V.; Sahnoun, R.; Neyman, K. M.; Rösch, N.; Hoffmann, J.; Schauermann, S.; Johánek, V.; Unterhalt, H.; Rupprechter, G.; Libuda, J.; Freund, H.-J. CO Adsorption on Pd Nanoparticles: Density Functional and Vibrational Spectroscopy Studies. *J. Phys. Chem. B* **2003**, *107*, 255−264.

(7) Nigra, M. M.; Arslan, I.; Katz, A. Gold Nanoparticle-Catalyzed Reduction in a Model System: Quantitative Determination of Reactive Heterogeneity of a Supported Nanoparticle Surface. *J. Catal.* **2012**, *295*, 115−121.

(8) Luo, Z.; Kriz, D. A.; Miao, R.; Kuo, C.-H.; Zhong, W.; Guild, C.; He, J.; Willis, B.; Dang, Y.; Suib, S. L.; Nandi, P. TiO_2 Supported gold-palladium catalyst for effective syngas production from methane partial oxidation. *Appl. Catal., A* **2018**, *554*, 54−63.

(9) Khorshidi, A.; Violet, J.; Hashemi, J.; Peterson, A. A. How Strain Can Break the Scaling Relations of Catalysis. *Nat. Catal.* **2018**, *1*, 263−268.

(10) Mavrikakis, M.; Hammer, B.; Nørskov, J. K. Effect of Strain on the Reactivity of Metal Surfaces. *Phys. Rev. Lett.* **1998**, *81*, 2819−2822.

(11) Reyes-Nava, J. A.; Rodríguez-López, J. L.; Pal, U. Generalizing Segregation and Chemical Ordering in Bimetallic Nanoclusters through Atomistic View Points. *Phys. Rev. B* **2009**, *80*, 161412.

(12) Xu, Y.; Mavrikakis, M. Adsorption and Dissociation of O_2 on Gold Surfaces: Effect of Steps and Strain. *J. Phys. Chem. B* **2003**, *107*, 9298−9307.

(13) Grabow, L. C.; Studt, F.; Abild-Pedersen, F.; Petzold, V.; Kleis, J.; Bligaard, T.; Nørskov, J. K. Descriptor-Based Analysis Applied to HCN Synthesis from NH_3 and CH_4. *Angew. Chem., Int. Ed.* **2011**, *50*, 4601−4605.

(14) Krug, R. R.; Hunter, W. G.; Grieger, R. A. Enthalpy-Entropy Compensation. 2. Separation of the Chemical from the Statistical Effect. *J. Phys. Chem.* **1976**, *80*, 2341−2351.

(15) Krug, R. R.; Hunter, W. G.; Grieger, R. A. Enthalpy-entropy compensation. 1. Some fundamental statistical problems associated with the analysis of van't Hoff and Arrhenius data. *J. Phys. Chem.* **1976**, *80*, 2335−2341.

(16) Khrapunov, S. The Enthalpy-Entropy Compensation Phenomenon. Limitations for the Use of Some Basic Thermodynamic Equations. *Curr. Protein Pept. Sci.* **2018**, *19*, 1088−1091.

(17) Perez-Benito, J. F. Some Tentative Explanations for the Enthalpy-Entropy Compensation Effect in Chemical Kinetics: From Experimental Errors to the Hinshelwood-like Model. *Monatsh. Chem.* **2013**, *144*, 49−58.

(18) Liu, L.; Guo, Q.-X. Isokinetic Relationship, Isoequilibrium Relationship, and Enthalpy−Entropy Compensation. *Chem. Rev.* **2001**, *101*, 673−696.

(19) Regalbuto, J. Catalyst Preparation: Science and Engineering. *Focus Catal.* **2007**, *2007*, 8.

(20) Wan, X.-K.; Wang, J.-Q.; Nan, Z.-A.; Wang, Q.-M. Ligand Effects in Catalysis by Atomically Precise Gold Nanoclusters. *Sci. Adv.* **2017**, *3*, No. e1701823.

(21) Tolman, C. A. Steric Effects of Phosphorus Ligands in Organometallic Chemistry and Homogeneous Catalysis. *Chem. Rev.* **1977**, *77*, 313−348.

(22) Johnson, G. E.; Laskin, J. Understanding Ligand Effects in Gold Clusters Using Mass Spectrometry. *Analyst* **2016**, *141*, 3573−3589.

(23) Wu, Z.; Jin, R. On the Ligand's Role in the Fluorescence of Gold Nanoclusters. *Nano Lett.* **2010**, *10*, 2568−2573.
(24) Mollenhauer, D.; Gaston, N. Phosphine Passivated Gold Clusters: How Charge Transfer Affects Electronic Structure and Stability. *Phys. Chem. Chem. Phys.* **2016**, *18*, 29686−29697.
(25) Forward, J. M.; Bohmann, D.; Fackler, J. P.; Staples, R. J. Luminescence Studies of Gold(I) Thiolate Complexes. *Inorg. Chem.* **1995**, *34*, 6330−6336.
(26) Wong, A.; Liu, Q.; Griffin, S.; Nicholls, A.; Regalbuto, J. R. Synthesis of Ultrasmall, Homogeneously Alloyed, Bimetallic Nanoparticles on Silica Supports. *Sci. 80* **2017**, *358*, 1427−1430.
(27) Pongthawornsakun, B.; Wimonsupakit, N.; Panpranot, J. Preparation of TiO_2 supported Au-Pd and Cu-Pd by the combined strong electrostatic adsorption and electroless deposition for selective hydrogenation of acetylene. *J. Chem. Sci.* **2017**, *129*, 1721−1734.
(28) Riyapan, S.; Zhang, Y.; Wongkaew, A.; Pongthawornsakun, B.; Monnier, J. R.; Panpranot, J. Preparation of improved Ag-Pd/TiO_2 catalysts using the combined strong electrostatic adsorption and electroless deposition methods for the selective hydrogenation of acetylene. *Catal. Sci. Technol.* **2016**, *6*, 5608−5617.
(29) Jiao, L.; Regalbuto, J. R. The Synthesis of Highly Dispersed Noble and Base Metals on Silica via Strong Electrostatic Adsorption: I. Amorphous Silica. *J. Catal.* **2008**, *260*, 329−341.
(30) Kang, X.; Wang, S.; Song, Y.; Jin, S.; Sun, G.; Yu, H.; Zhu, M. Bimetallic Au_2Cu_6 Nanoclusters: Strong Luminescence Induced by the Aggregation of Copper(I) Complexes with Gold(0) Species. *Angew. Chem., Int. Ed.* **2016**, *55*, 3611−3614.
(31) Lu, Y.; Chen, W. Sub-Nanometre Sized Metal Clusters: From Synthetic Challenges to the Unique Property Discoveries. *Chem. Soc. Rev.* **2012**, *41*, 3594−3623.
(32) de Silva, N.; Ha, J.-M.; Solovyov, A.; Nigra, M. M.; Ogino, I.; Yeh, S. W.; Durkin, K. A.; Katz, A. A Bioinspired Approach for Controlling Accessibility in Calix[4]Arene-Bound Metal Cluster Catalysts. *Nat. Chem.* **2010**, *2*, 1062−1068.
(33) Okumura, M.; Haruta, M.; Kitagawa, Y.; Yamaguchia, K. Theoretical Study of H_2O and O_2 Adsorption on Au Small Clusters. *Gold Bull.* **2007**, *40*, 40−44.
(34) Okumura, M.; Kitagawa, Y.; Haruta, M.; Yamaguchi, K. DFT Studies of Interaction between O_2 and Au Clusters. The Role of Anionic Surface Au Atoms on Au Clusters for Catalyzed Oxygenation. *Chem. Phys. Lett.* **2001**, *346*, 163−168.
(35) Liu, X.; Atwater, M.; Wang, J.; Huo, Q. Extinction Coefficient of Gold Nanoparticles with Different Sizes and Different Capping Ligands. *Colloids Surf., B* **2007**, *58*, 3−7.
(36) Noguez, C. Surface Plasmons on Metal Nanoparticles: The Influence of Shape and Physical Environment. *J. Phys. Chem. C* **2007**, *111*, 3806−3819.
(37) Amendola, V.; Pilot, R.; Frasconi, M.; Maragò, O. M.; Iatì, M. A. Surface Plasmon Resonance in Gold Nanoparticles: A Review. *J. Phys.: Condens. Matter* **2017**, *29*, 203002.
(38) Amendola, V.; Meneghetti, M. Size Evaluation of Gold Nanoparticles by UV−vis Spectroscopy. *J. Phys. Chem. C* **2009**, *113*, 4277−4285.
(39) Hostetler, M. J.; Wingate, J. E.; Zhong, C.-J.; Harris, J. E.; Vachet, R. W.; Clark, M. R.; Londono, J. D.; Green, S. J.; Stokes, J. J.; Wignall, G. D.; Glish, G. L.; Porter, M. D.; Evans, N. D.; Murray, R. W. Alkanethiolate Gold Cluster Molecules with Core Diameters from 1.5 to 5.2 nm: Core and Monolayer Properties as a Function of Core Size. *Langmuir* **1998**, *14*, 17−30.
(40) Ab Rahim, M. H.; Armstrong, R. D.; Hammond, C.; Dimitratos, N.; Freakley, S. J.; Forde, M. M.; Morgan, D. J.; Lalev, G.; Jenkins, R. L.; Lopez-Sanchez, J. A.; Taylor, S. H.; Hutchings, G. J. Low Temperature Selective Oxidation of Methane to Methanol Using Titania Supported Gold Palladium Copper Catalysts. *Catal. Sci. Technol.* **2016**, *6*, 3410−3418.
(41) Nabika, H.; Mizuhata, M.; Kajinami, A.; Deki, S.; Akamatsu, K. Preparation and Characterization of Au/Co Nano-Alloys. *J. Electroanal. Chem.* **2003**, *559*, 99−102.
(42) Okamoto, H.; Massalski, T. B. The Au-Ru (Gold-Ruthenium) System. *Bull. Alloy Phase Diagrams* **1984**, *5*, 388−390.
(43) Barndõk, H.; Merayo, N.; Blanco, L.; Hermosilla, D.; Blanco, Á. Application of On-Line FTIR Methodology to Study the Mechanisms of Heterogeneous Advanced Oxidation Processes. *Appl. Catal., B* **2016**, *185*, 344−352.
(44) Armaroli, T.; Bécue, T.; Gautier, S. Diffuse Reflection Infrared Spectroscopy (DRIFTS): Application to the in Situ Analysis of Catalysts. *Oil Gas Sci. Technol.* **2004**, *59*, 215−237.
(45) Gaur, S.; Wu, H.; Stanley, G. G.; More, K.; Kumar, C. S. S. R.; Spivey, J. J. CO oxidation studies over cluster-derived Au/TiO_2 and AUROlite Au/TiO_2 catalysts using DRIFTS. *Catal. Today* **2013**, *208*, 72−81.
(46) Tang, H.; Su, Y.; Zhang, B.; Lee, A. F.; Isaacs, M. A.; Wilson, K.; Li, L.; Ren, Y.; Huang, J.; Haruta, M.; Qiao, B.; Liu, X.; Jin, C.; Su, D.; Wang, J.; Zhang, T. Classical strong metal-support interactions between gold nanoparticles and titanium dioxide. *Sci. Adv.* **2017**, *3*, No. e1700231.
(47) Evans, J.; Hayden, B. E.; Lu, G. The Adsorption of Carbon Monoxide on TiO_2(110) Supported Palladium. *Surf. Sci.* **1996**, *360*, 61−73.
(48) Kapil, N.; Weissenberger, T.; Cardinale, F.; Trogadas, P.; Nijhuis, T. A.; Nigra, M. M.; Coppens, M.-O. Precisely Engineered Supported Gold Clusters as a Stable Catalyst for Propylene Epoxidation. *Angew. Chem., Int. Ed.* **2021**, *60*, 18185−18193.

https://doi.org/10.1021/acsomega.1c04236
ACS Omega 2021, 6, 24269−24279